


 Cite this: *RSC Adv.*, 2024, 14, 34746

# Efficient adsorption performance of uranium in wastewater by novel MXene material TiVCT<sub>x</sub> and its aerogel composites†

 Xiaoxia Luo,<sup>\*a</sup> Xianliang Ren<sup>b</sup> and Hongwei Wang<sup>©\*bc</sup>

This work focuses on the application potential of novel MXene materials in the field of uranium-containing wastewater adsorption, particularly addressing gaps in existing research. Ultra-thin layered TiVCT<sub>x</sub> was selected as the core adsorbent to thoroughly investigate its adsorption performance of uranium(U(VI))-containing wastewater. By compounding with sodium alginate, we successfully prepared easily recoverable aerogel beads and evaluated their adsorption capacity for ultra-low concentrations of U(VI) in seawater. The findings of this study reveal that TiVCT<sub>x</sub> exhibits optimal adsorption capacity for U(VI) in a weakly acidic environment with a pH of 5.59, and its maximum adsorption capacity for U(VI) reaches up to 336 mg g<sup>-1</sup>, demonstrating superior performance when it comes to other MXene materials. Further research reveals that the adsorption mechanism involves the synergistic effect of electrostatic adsorption and reduction adsorption, exhibiting monolayer adsorption characteristics, and the adsorption process is a spontaneous endothermic reaction. Notably, in simulated complex seawater environments, even when the U(VI) concentration is as low as, for instance, 3.3 μg L<sup>-1</sup>, 50 mg of aerogel beads can still achieve an adsorption capacity of 3.89 mg g<sup>-1</sup> for 60 L of seawater. These findings underscore the outstanding performance of TiVCT<sub>x</sub> as a novel MXene material in U(VI) adsorption and its broad potential for practical applications.

 Received 30th July 2024  
 Accepted 19th October 2024

DOI: 10.1039/d4ra05531d

[rsc.li/rsc-advances](https://rsc.li/rsc-advances)

## 1. Introduction

With the ongoing advancements in nuclear energy technology, the issue of nuclear wastewater has become increasingly prominent, and its potential hazards cannot be overlooked.<sup>1,2</sup> The radioactive substances contained within nuclear wastewater not only have the potential to induce cellular mutations and genetic information damage but also significantly elevate the risk of malignant diseases, including cancer.<sup>3,4</sup> Even more severe is the fact that, upon infiltrating natural water bodies, these radioactive wastewaters can cause long-term and severe harm to aquatic organisms through the cumulative effects of the food chain, ultimately posing a fatal threat to the entire ecosystem. In addressing the challenges posed by nuclear wastewater treatment, various methods have been widely employed, including precipitation, oxidation–reduction, electrodialysis, bioreduction, and adsorption.<sup>5,6</sup> Among these,

adsorption occupies a significant position in the field of nuclear wastewater treatment due to its multiple advantages, such as high efficiency, flexibility, environmental friendliness, and cost-effectiveness, and it has garnered extensive industrial application.<sup>7</sup> The tunable pore structure demonstrates extensive application potential in the field of adsorption and separation. As an emerging two-dimensional material, MXene's layered structure, composed of transition metal elements and elements such as carbon and nitrogen, confers upon it remarkable chemical stability and a substantial specific surface area.<sup>8</sup> The surface of MXene is rich in functional groups such as hydroxyl and oxo groups, providing abundant adsorption active sites. These unique properties endow MXene with significant advantages in the treatment of U(VI)-containing nuclear wastewater.<sup>9</sup> The adsorption capacity of monolayer Ti<sub>3</sub>C<sub>2</sub>T<sub>x</sub> for U(VI) can reach 214 mg g<sup>-1</sup>,<sup>10</sup> while that of monolayer Ti<sub>2</sub>CT<sub>x</sub> is even higher, achieving 470 mg g<sup>-1</sup>,<sup>11</sup> which is 2.2 times that of Ti<sub>3</sub>C<sub>2</sub>T<sub>x</sub>. Further modification, such as carboxyl-functionalized Ti<sub>3</sub>C<sub>2</sub>T<sub>x</sub> (TCCH), can enhance its adsorption capacity for U(VI) to 334 mg g<sup>-1</sup>.<sup>12</sup> Zhao *et al.* made an in-depth study on benzoyl thiourea-fixed activated carbon (BT-AC), and discussed its preparation process and adsorption mechanism for U(VI). The mechanism of BT-AC removal of U(VI) mainly depends on the coordination between U(VI) and the O, S and N atoms in BT-AC. In the environment of competitive ion coexistence, BT-AC can still maintain the selective adsorption of U(VI), and the adsorption capacity reaches 82 mg g<sup>-1</sup>.<sup>13</sup> Bai *et al.* developed

<sup>a</sup>Chongqing College of Mobile Communication, Chongqing, 401520, P. R. China. E-mail: xiaoxialuo90@163.com

<sup>b</sup>National Key Laboratory of Advanced Casting Technologies, Chongqing Key Laboratory of Soft Condensed Matter Physics and Smart Materials, College of Physics, Chongqing University, Chongqing, 400044, P. R. China. E-mail: 20202701013@cqu.edu.cn

<sup>c</sup>Department of Ultrasound, Xinqiao Hospital, Army Medical University (Third Military Medical University), Chongqing, 400044, P. R. China

† Electronic supplementary information (ESI) available. See DOI: <https://doi.org/10.1039/d4ra05531d>



a porous resin (HCR-CO) through structural design of hydroxyphenylacetonitrile modified resin.<sup>14</sup> The high specific surface area and abundant micropores of HCR-AO can accelerate the diffusion of  $U(vi)$  at the outer surface adsorption stage. The maximum adsorption capacity of HCR-AO for  $U(vi)$  is 380 mg  $g^{-1}$ , and the adsorption capacity of HCR-AO is still excellent after 8 cycles. Existing research has fully demonstrated the excellent performance of MXene in  $U(vi)$ -containing wastewater treatment. However, current research primarily focuses on the two mature MXene materials,  $Ti_3C_2T_x$  and  $Ti_2CT_x$ , with relatively scarce reports on novel MXene, indicating significant research gaps that hinder researchers' deep exploration of MXene's adsorption mechanisms. In fact, over 30 types of MXene have been successfully synthesized,<sup>15</sup> among which  $TiVCT_x$ , as a relatively new  $M_2X$ -type MXene material, shares similar composition and structure with  $Ti_2CT_x$  and exhibits stronger reduction performance, promising to be a more potential novel adsorbent for nuclear wastewater.<sup>16</sup> Furthermore, after treating nuclear wastewater as an adsorbent, MXene faces separation challenges, requiring complex separation methods such as vacuum filtration and high-speed centrifugation to achieve effective separation of adsorbed products, which greatly limits its practical application.<sup>17</sup> Therefore, designing and synthesizing MXene adsorbent materials that are easy to recover and separate is a pressing scientific challenge. In this study, a new MXene- $TiVCT_x$  with  $M_2XT_x$  configuration was selected as the  $U(vi)$  adsorbent. The doping of V not only makes the MXene of this composition more active, but also provides a reduction adsorption site for  $U(vi)$  adsorption, which improves the  $U(vi)$  adsorption capacity of MXene. It also provides a new way to develop high performance MXene adsorbents.

In the context of this research, the present study selected the novel MXene material  $TiVCT_x$  as an adsorbent and systematically investigated its adsorption performance and mechanism for  $U(vi)$ -containing wastewater. The specific research content encompassed examining the effects of environmental factors such as pH value, temperature, and interfering ions on the adsorption performance of  $TiVCT_x$ , and subsequently determining the optimal environmental conditions for its application. Furthermore, this study successfully synthesized  $TiVCT_x$  composite sodium alginate aerogel beads that are easy to recover and separate, which demonstrated high adsorption capacity for extremely low concentrations of  $U(vi)$  in simulated seawater environments.

## 2. Experimental

### 2.1 Materials

The precursor  $TiVAlC$  was purchased from Beike Nanometer, while uranyl was obtained from Aladdin.  $HCl$ ,  $HNO_3$ ,  $NaOH$ ,  $LiF$ ,  $NaCl$ ,  $CaCl_2$ ,  $KCl$ ,  $Na_2SO_4$ , and  $MgSO_4$  were purchased from Sinopharm Chemical Reagent Co., Ltd.

### 2.2 Preparation of $TiVCT_x$

$TiVCT_x$  was prepared by etching the precursor  $TiVAlC$  with a mixed solution of  $LiF$  and  $HCl$ . The procedure involved mixing

1.6 g of  $LiF$  and 20 mL of 9 M  $HCl$  to create the etching solution, adding 1 g of  $TiVAlC$  powder, and etching at 45 °C for 48 h. Post-etching, the mixture was washed, ultrasonicated, and centrifuged. The supernatant was collected, yielding the  $TiVCT_x$  solution, which was then freeze-dried to obtain the  $TiVCT_x$  powder.

### 2.3 Preparation of $TiVCT_x@SA$ aerogel

A 100 mL solution of  $TiVCT_x$  with a concentration of 4.56 mg  $mL^{-1}$  was prepared. Then, 2 g of sodium alginate was added, and the mixture was vigorously stirred for 20 min until a uniform colloidal state was reached. The colloidal mixture was dropwise added into a 2 wt%  $CaCl_2$  solution and allowed to crosslink for 5 h. After vacuum freeze-drying, the  $TiVCT_x@SA$  aerogel was obtained. The preparation process diagram is shown in Fig. 1.

### 2.4 Batch adsorption experiments

$U(vi)$  solutions with varying concentrations were prepared by dissolving uranyl in ultrapure water. During the adsorption process, 20 mg of  $TiVCT_x$  was utilized, with a  $U(vi)$  solution volume of 100 mL, under magnetic stirring at a rate of 600 rpm. With the exception of thermodynamic experiments, all experiments were conducted at a controlled temperature of 25 °C. Unless otherwise specified for pH-related experiments, the pH was maintained at the optimal adsorption value of 5. To simulate low-concentration  $U(vi)$  adsorption in seawater, the seawater environment was formulated according to the Moeledon synthetic seawater recipe (ESI Table S1†), with a pH of 8.3 and a  $U(vi)$  concentration of 3.3  $\mu g L^{-1}$ .

The adsorption capacity and removal efficiency at various time points are determined using eqn (1)–(3):<sup>16</sup>

$$q_t = \frac{(C_0 - C_t)V}{m} \quad (1)$$

$$q_e = \frac{(C_0 - C_e)V}{m} \quad (2)$$

$$R\% = \frac{C_0 - C_e}{C_0} \times 100\% \quad (3)$$

The adsorption capacities (mg  $g^{-1}$ ) at time  $t$  and equilibrium are denoted as  $q_t$  and  $q_e$ , respectively.  $C_0$  (mg  $L^{-1}$ ) represents the initial concentration of  $U(vi)$ ,  $C_t$  (mg  $L^{-1}$ ) denotes the concentration at time  $t$ , and  $C_e$  signifies the concentration at equilibrium.  $V$  denotes the volume (L) of the  $U(vi)$  solution, while  $m$  represents the mass (g) of the adsorbent, and  $R$  represents the removal efficiency (%).<sup>18</sup>

The fitting formulas of the pseudo-first-order kinetic model, pseudo-second-order kinetic model and Weber diffusion model are as follows:

$$\log(q_e - q_t) = \log q_e - \frac{k_1}{2.303} \times t \quad (4)$$

$$\frac{t}{q_t} = \frac{1}{k_2 q_e^2} + \frac{t}{q_e} \quad (5)$$



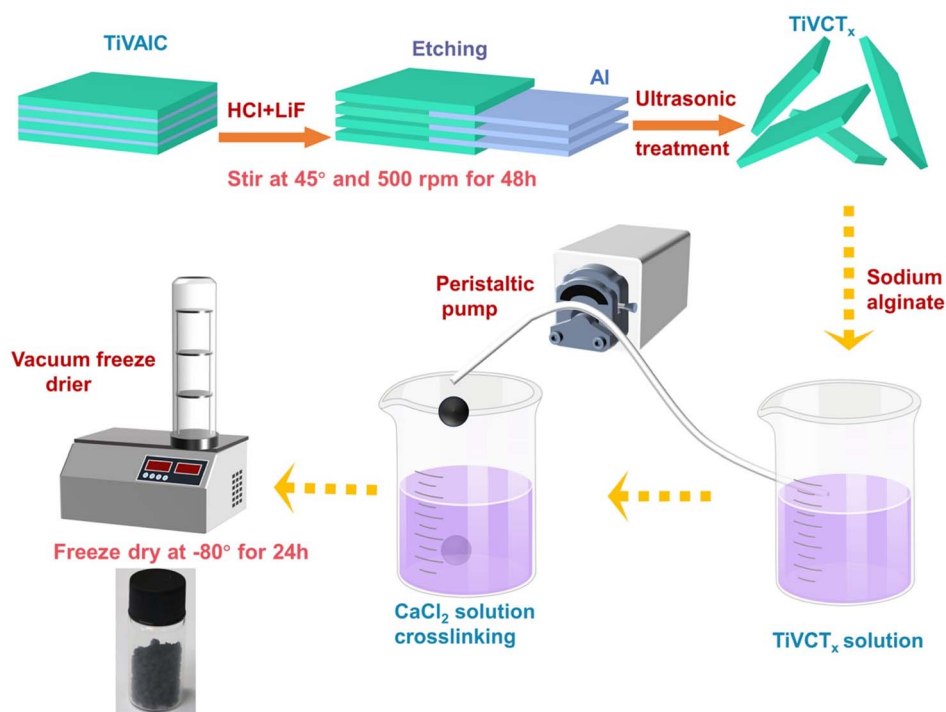


Fig. 1 Preparation process of MXene materials and aerogel composites diagram.

$$q_t = k_i t^{\frac{1}{2}} + C_i \quad (6)$$

$k_1$  ( $\text{min}^{-1}$ ) and  $k_2$  ( $\text{g min}^{-1} \text{mg}^{-1}$ ) represent the adsorption rate constants,  $k_i$  denotes the coefficient of phase  $i$  in Weber's model.<sup>19</sup>

The Langmuir and Freundlich isotherm models are derived from the following equations:<sup>20</sup>

$$\frac{C_e}{q_e} = \frac{1}{K_1 q_m} + \frac{C_e}{q_m} \quad (7)$$

$$\ln q_e = \ln K_f + \frac{1}{n} \ln C_e \quad (8)$$

$q_m$  ( $\text{mg g}^{-1}$ ) denotes maximum adsorption capacity;  $K_1$  represents Langmuir constants related to adsorption energy;  $K_f$  is Freundlich model constant;  $n$  is Freundlich exponent for sorption intensity. Eqn (4)–(8) correspond to a quasi-first-order kinetic model, a quasi-second-order kinetic model, a Weber diffusion model, a Langmuir adsorption isotherm model and a Freundlich adsorption isotherm model.

The formulas for entropy ( $\Delta S$ ), enthalpy ( $\Delta H$ ), and Gibbs free energy ( $\Delta G$ ) are presented below:<sup>21</sup>

$$K_d = \frac{(C_0 - C_e)V}{mC_e} \quad (9)$$

$$\ln K_d = \frac{\Delta S}{R} - \frac{\Delta H}{RT} \quad (10)$$

$$\Delta G = \Delta H - T \times \Delta S \quad (11)$$

where  $K_d$  is the distribution coefficient ( $\text{mL g}^{-1}$ ),  $R$  stands for the gas rate constant ( $8.314 \text{ J mol}^{-1} \text{ K}^{-1}$ ),  $T$  is temperature in kelvin (K).

## 2.5 Desorption

In this study, a mixture of hydrochloric acid and nitric acid was used as the desorption agent for  $\text{TiVCT}_x$ . The adsorbed solution was centrifuged at 8000 rpm for 30 min, and the  $\text{TiVCT}_x$  nanosheets were separated precipitated and collected. Add 20 mL 5 M HCl and 5 M  $\text{HNO}_3$  into the mixture and stir magnetically at room temperature for 6 h; after washing with deionized water, adjust the pH to 6.5 with 0.1 mol per L NaOH, and then stir for 2 h; the precipitation was obtained by centrifugation at 8000 rpm for 30 min, freeze-dried, and then further adsorbed.

## 2.6 Characterization

X-ray diffractometer (X'Pert Powder X, PANalytical) was used to analyze the crystal structure of the sample, the testing angle is  $5\text{--}90^\circ$ , the scanning speed is  $2^\circ \text{ min}^{-1}$ , and the scanning electron microscope (JSM-6800F, JEOL) was used to detect the morphology of the sample. The zeta potential analyzer (Nano-brook Omni, Brookhaven) evaluates the surface charge of the sample, and the X-ray photoelectron spectrometer (ESCALAB 250Xi, Thermo Fisher Scientific) measures the binding energy and valence change of the sample. Ion concentration was measured using an inductively coupled plasma emission spectrometer (PerkinElmer 8300).



### 3. Result and discussion

#### 3.1 Characterization of TiVCT<sub>x</sub>

As depicted in Fig. 2A, the XRD pattern clearly reveals that the diffraction peak corresponding to Al (103) in TiVAIC vanishes completely after the etching process, providing compelling evidence for the successful removal of the Al element. Concurrently, it is observed that the (002) diffraction peak of etched TiVCT<sub>x</sub> shifts towards smaller angles, indicating an increase in lattice spacing as a result of the etching process.<sup>22</sup> Fig. 2B illustrates the variation of the zeta potential of TiVCT<sub>x</sub> under different pH conditions. The point of zero charge (PZC) of TiVCT<sub>x</sub> is 2.29. When the environmental pH is below 2.29, the potential of TiVCT<sub>x</sub> exhibits a positive value; whereas, when the pH exceeds 2.29, its potential shifts to a negative value. Investigating the zeta potential of TiVCT<sub>x</sub> paves the way for a deeper exploration of the mechanism by which pH influences adsorption processes.<sup>23</sup> Fig. 2C and D respectively exhibit the N<sub>2</sub> adsorption–desorption curves for TiVCT<sub>x</sub> and TiVCT<sub>x</sub>@SA aerogel. The BET specific surface area of TiV is found to be 6.01 m<sup>2</sup> g<sup>-1</sup>, indicating an excellent standing within the MXene family.<sup>24</sup> By contrast, the BET specific surface area of the TiVCT<sub>x</sub>@SA aerogel attains 17.28 m<sup>2</sup> g<sup>-1</sup>, marking a significant enhancement of more than twofold relative to TiVCT<sub>x</sub>. This attribute is particularly conducive to augmenting its adsorption capabilities.

The SEM images (Fig. 3A and B) showed that the precursor TiVAIC had a massive structure of 14 × 11 μm, while the etched TiVCT<sub>x</sub> had a layered structure of 13 × 10 μm. It is the size of a typical TiVCT<sub>x</sub> slice and is universal, with a small number of smaller TiVCT<sub>x</sub> slices available. Through AFM testing (Fig. 3C), it is determined that the thickness of TiVCT<sub>x</sub> is approximately 2 nm (Fig. 3D), thereby confirming its ultra-thin nanolayer nature. The TiVCT<sub>x</sub>@SA aerogel spheres possess a diameter of 1.88 μm, and their cross-sectional SEM image reveals an internal structure reminiscent of a honeycomb, composed of numerous pores (Fig. 3F). Upon further SEM magnification, it is revealed that the interior of these spheres is comprised of thin layered structures (Fig. 3G). Lastly, Fig. 3H provides a visual representation of the TiVCT<sub>x</sub>@SA aerogel.

#### 3.2 U(vi) adsorption properties of TiVCT<sub>x</sub>

**3.2.1 Effect of pH.** To determine the optimal conditions for the application of TiVCT<sub>x</sub> in adsorbing U(vi), this study investigated the adsorption capacity of TiVCT<sub>x</sub> across different pH environments. Initially, pure NaOH was utilized to adjust the pH of the U(vi) solution, effectively eliminating any potential influence of NaOH on the adsorption results (ESI Fig. S1†). As the pH increased from 2 to 11, the adsorption capacity of TiVCT<sub>x</sub> exhibited an initial rise followed by a decline. The maximum adsorption capacity was observed at a pH of 5.59, reaching 239 mg g<sup>-1</sup> (Fig. 4A). The study further calculated the

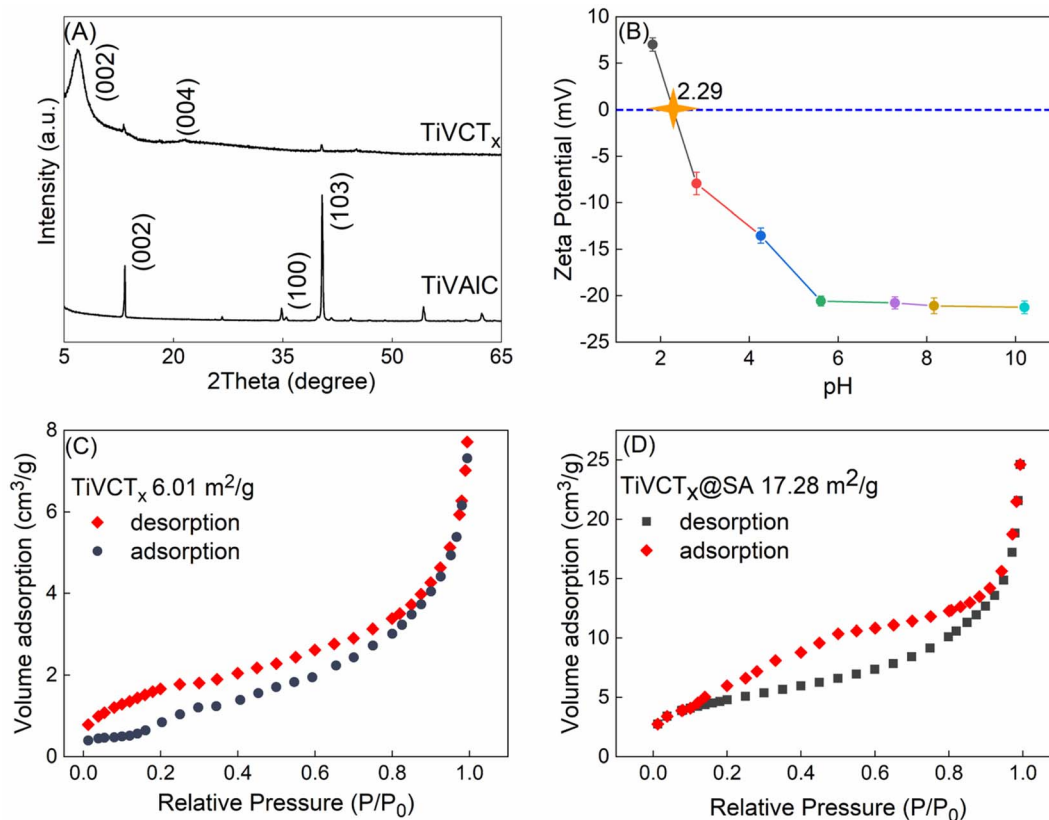


Fig. 2 (A) XRD pattern of TiVCT<sub>x</sub>; (B) zeta potential diagram of TiVCT<sub>x</sub> at different pH values; (C) N<sub>2</sub> adsorption–desorption curve of (C) TiVCT<sub>x</sub> and (D) TiVCT<sub>x</sub>@SA aerogel.



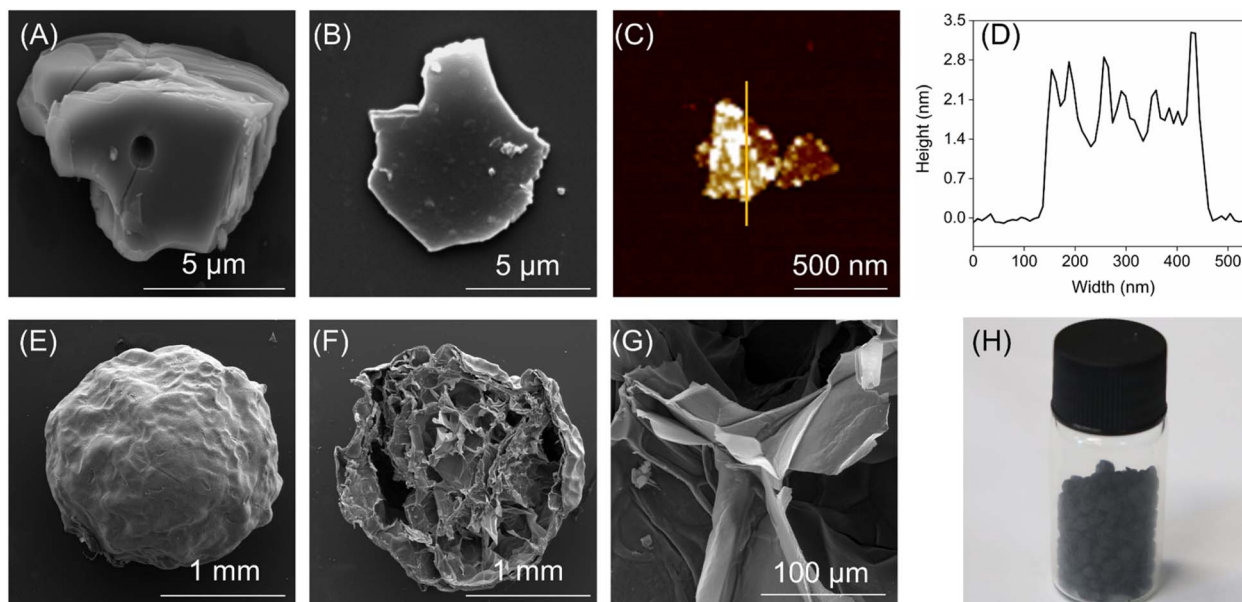


Fig. 3 (A) SEM image of TiVAIC; (B) SEM, (C) AFM, and (D) AFM thickness images of TiVCT<sub>x</sub>, respectively; (E) SEM, (F) cross-sectional SEM, (G) internal SEM, and (H) physical image of TiVCT<sub>x</sub>@SA aerogel.

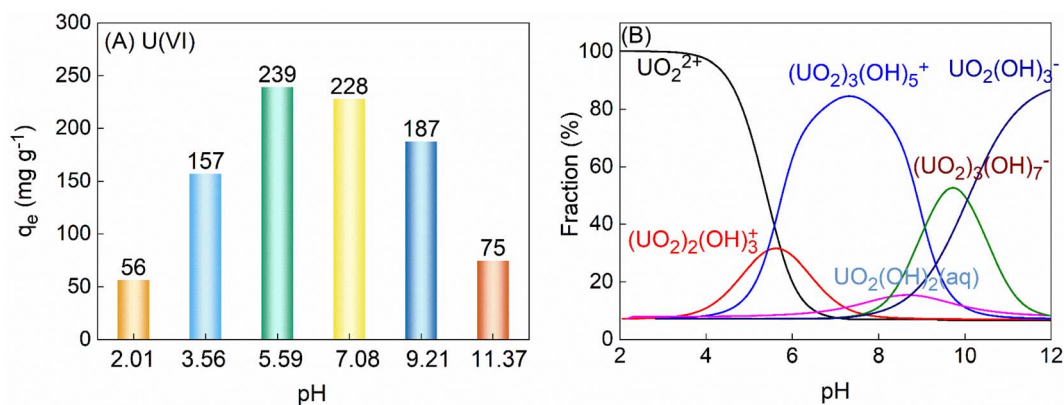


Fig. 4 (A) The adsorption capacity of 100 mL 125 mg per L U(vi) adsorbed by 50 mg TiVCT<sub>x</sub> varies with pH; (B) the form of U present varies with pH.

speciation of U at various pH values, as depicted in Fig. 4B. By analyzing the zeta potential of TiVCT<sub>x</sub> alongside the speciation of U, the mechanism underlying the influence of pH on the adsorption by TiVCT<sub>x</sub> was further elucidated. At pH values below 2.29, TiVCT<sub>x</sub> carries a positive charge and experiences electrostatic repulsion with positively charged UO<sub>2</sub><sup>2+</sup>, resulting in a low adsorption capacity. Conversely, when the pH exceeds 2.29, TiVCT<sub>x</sub> becomes negatively charged and attracts positively charged UO<sub>2</sub><sup>2+</sup> via electrostatic attraction.<sup>25</sup> As the negative charge of TiVCT<sub>x</sub> gradually intensifies, the electrostatic attraction strengthens, subsequently leading to an increase in adsorption capacity. However, as the pH continues to rise above 7.1, UO<sub>2</sub><sup>2+</sup> combines with a substantial amount of OH and begins to carry a negative charge. At this juncture, the negative charge of TiVCT<sub>x</sub> is nearly maximized, causing electrostatic repulsion between TiVCT<sub>x</sub> and U(vi), which ultimately leads to a decrease in adsorption capacity. Given that the optimal pH

environment for the application of TiVCT<sub>x</sub> in adsorbing U(vi) is under weakly acidic conditions, the pH was uniformly set at 5.6 in the subsequent adsorption experiments.

**3.2.2 Adsorption kinetics and isotherm.** To delve into the adsorption process, this study investigated the relationship between adsorption capacity and time. The experimental results indicated that TiVCT<sub>x</sub> achieved over 80% of its equilibrium adsorption capacity within the initial 10 min and reached full adsorption equilibrium at 60 min, with no subsequent increase in adsorption capacity. To further elucidate the adsorption mechanism, pseudo-first-order and pseudo-second-order kinetic models were employed to fit the experimental data (as shown in Fig. 5A). The findings revealed that the pseudo-second-order kinetic model exhibited a correlation coefficient of up to 99% with the experimental data. Moreover, the theoretical equilibrium adsorption capacity derived from this model, calculated using the fitting parameters in Table 1, was in



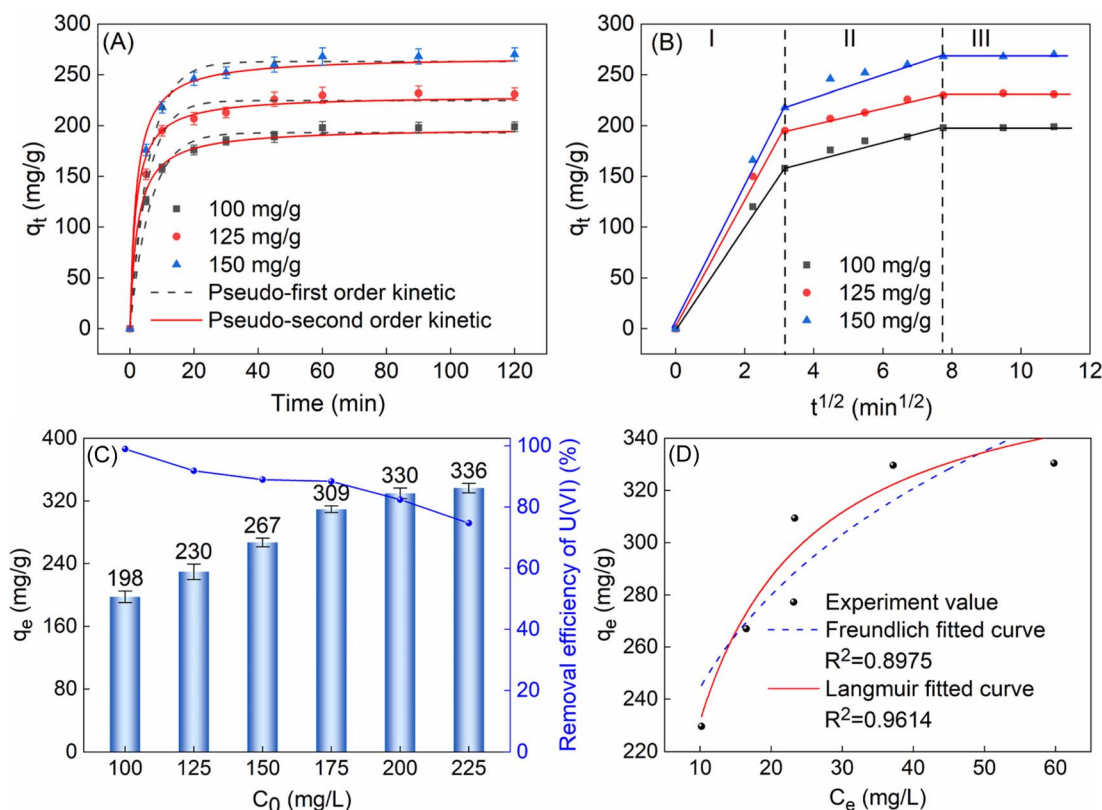


Fig. 5 (A) The  $q_t$  of 50 mg TiVCT<sub>x</sub> adsorbing 100, 125 and 150 mg per L U(vi) with time; (B) intragranular diffusion model; (C) the  $q_e$  of 50 mg TiVCT<sub>x</sub> varies with the initial concentration of U(vi); (D) Freundlich and Langmuir isotherm fit curves.

Table 1 Fitting results of PFO kinetics and PSO kinetics

Adsorbate	$C_0$ (mg L <sup>-1</sup> )	$q_{e \text{ exp}}$ (mg g <sup>-1</sup> )	Pseudo-first-order model			Pseudo-second-order model		
			$q_{e \text{ cal}}$ (mg g <sup>-1</sup> )	$k_1$	$R^2$	$q_{e \text{ cal}}$ (mg g <sup>-1</sup> )	$k_2$	$R^2$
U	100	198	193.32	0.36	0.99	198.69	0.02	0.99
	125	230	225.96	0.43	0.96	229.36	0.02	0.99
	150	267	263.53	0.38	0.95	266.14	0.01	0.98

closer agreement with the experimental results. It shows that the adsorption process is more consistent with the quasi-second-order kinetic model, which indicates that the adsorption process is mainly chemisorption.<sup>26</sup>

Furthermore, analysis using the intraparticle diffusion model revealed that the adsorption process consisted of three stages: the first 10 min represented the external diffusion stage, during which U(vi) rapidly diffused to the outer surface of TiVCT<sub>x</sub> and underwent adsorption reactions; the period from 10 to 60 min corresponded to the intraparticle diffusion stage, where, as the outer surface adsorption gradually saturated, U(vi) began to penetrate into the TiVCT<sub>x</sub> layers and undergo intraparticle diffusion and adsorption. After 60 min, adsorption and desorption reached a dynamic equilibrium, resulting in stabilized adsorption capacity. In conclusion, this adsorption process is a heterogeneous diffusion process governed by both external and intraparticle diffusion.<sup>27</sup>

To delve into the adsorption behavior on the surface of TiVCT<sub>x</sub> adsorbent, this study examined its adsorption capacity under different concentrations of U(vi) solutions. The experimental results revealed that as the initial concentration of U(vi) increased, the  $q_e$  gradually augmented. When the concentration reached 225 mg L<sup>-1</sup>, the adsorption capacity tended to saturate and ceased to increase significantly (Fig. 5C). The error bar is the standard error representing the range of error between the sample mean and the population after multiple experimental tests. The maximum adsorption capacity of 50 mg of TiVCT<sub>x</sub> was determined to be 336 mg g<sup>-1</sup>. By fitting the experimental results to both the Freundlich model and the Langmuir model (Fig. 5D), it was found that the Langmuir model exhibited a higher degree of fit, indicating that the adsorption process on the surface of TiVCT<sub>x</sub> was monolayer.<sup>28</sup>

**3.2.3 Adsorption thermodynamics.** This study investigated the impact of temperature on the adsorption capacity of TiVCT<sub>x</sub>



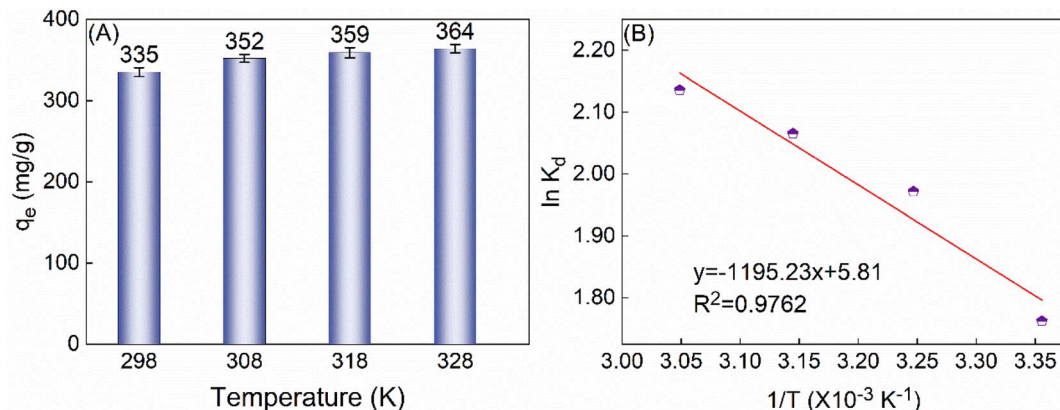


Fig. 6 (A) The  $q_e$  of 225 mg per L U(vi) by 50 mg TiVCT<sub>x</sub> varies with temperature; (B) thermodynamic equilibrium constant fitting diagram.

Table 2 Thermodynamic parameters of U(VI) adsorption by TiVCT<sub>x</sub>

Adsorbate	$\Delta H$ (kJ mol <sup>-1</sup> )	$\Delta S$ (J mol <sup>-1</sup> K <sup>-1</sup> )	$\Delta G$ (kJ mol <sup>-1</sup> )			
			298 K	308 K	318 K	328 K
U	9.94	48.30	-4.46	-4.94	-5.42	-5.91

at temperatures of 298, 308, and 318 K. The findings reveal that as the temperature rises, the  $q_e$  gradually increases (Fig. 6A), indicating that the adsorption process is endothermic. Further analysis of the thermodynamic equilibrium constant fitting plot (Fig. 6B) and the relevant thermodynamic parameters derived from the fitting results (Table 2) reveals that the adsorption process exhibits an endothermic nature ( $\Delta H > 0$ ) and results in an increase in the system's disorder ( $\Delta S > 0$ ).<sup>29</sup> However, owing

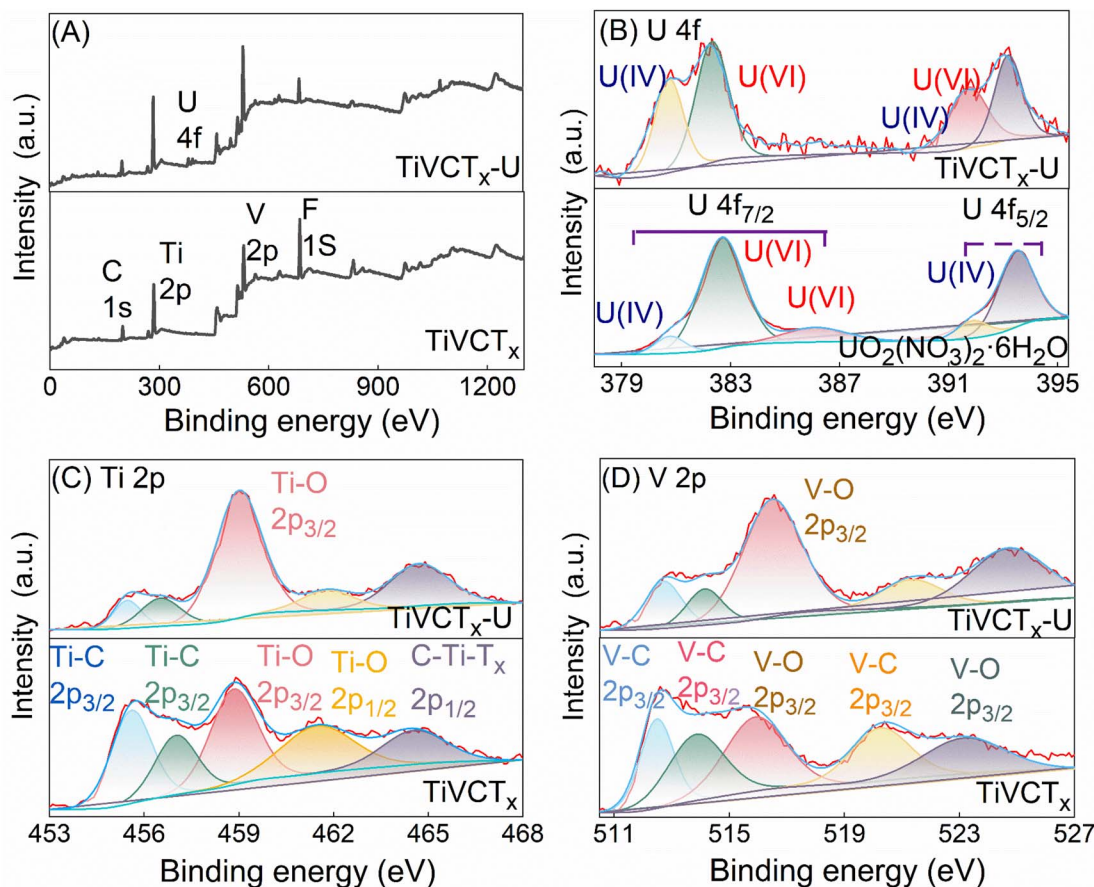


Fig. 7 XPS spectra before and after TiVCT<sub>x</sub> adsorbs U(vi): (A) survey scan spectrum, (B) high-resolution U 4f spectrum, (C) high-resolution Ti 2p spectrum, (D) high-resolution V 2p spectrum.



to the Gibbs free energy change ( $\Delta G$ ) being less than 0, the adsorption process can still proceed spontaneously.

### 3.3 Adsorption mechanism

This study analyzed the changes in binding energies of U, Ti, and O elements in TiVCT<sub>x</sub> before and after U(vi) adsorption using XPS tests, and the test results were shown in Fig. 7. The full spectrum scanning results indicated the presence of Ti, C, V, O, and F elements in TiVCT<sub>x</sub> before adsorption, while the emergence of U 4f peaks was observed after adsorption. High-resolution spectra further revealed that the pure uranyl species on the surface of TiVCT<sub>x</sub> before adsorption consisted of U(IV) and U(VI) for both 4f<sub>7/2</sub> and 4f<sub>5/2</sub> levels, with U(IV) accounting for 20.75% and U(VI) accounting for 75.25%. After adsorption, the proportions of U(IV) and U(VI) changed to 38.25% and 61.75%, respectively, indicating the reduction of U(VI) during the adsorption process.<sup>28</sup> Meanwhile, high-resolution spectra of Ti 2p and V 2p showed an increase in the proportions of Ti–O 2p<sub>3/2</sub> and V–O 2p<sub>3/2</sub> after U adsorption, suggesting that some Ti and V were oxidized during the adsorption process.<sup>11</sup> Comprehensive analysis demonstrates that reductive adsorption occurs during the adsorption of U(vi) by TiVCT<sub>x</sub>, which has also been reported in other MXenes.<sup>11,30,31</sup>

Based on the combined analysis of zeta potential, adsorption kinetic model fitting, and XPS results, the adsorption

mechanism is elucidated as follows: at a pH of approximately 5.59, the surface of TiVCT<sub>x</sub> carries a significant amount of negative charge, facilitating electrostatic adsorption with positively charged U(vi). Simultaneously, a small portion of U(vi) is reduced by unsaturated Ti and V in TiVCT<sub>x</sub>, leading to reductive adsorption. This mechanism, which involves both physical and chemical adsorption, confers excellent adsorption capacity to TiVCT<sub>x</sub>. As shown in the Table 3, when compared to other MXene adsorbents, TiVCT<sub>x</sub> exhibits a leading adsorption capacity.

### 3.4 Application of TiVCT<sub>x</sub>@SA aerogel in U(vi) adsorption from seawater

When investigating the actual adsorption effectiveness of TiVCT<sub>x</sub> towards low-concentration U(vi) in seawater, given the complexity of the marine environment and the low concentration of U(vi) (merely 3.3 μg L<sup>-1</sup>), we prepared easily recoverable TiVCT<sub>x</sub> aerogel beads and applied them to the study of U(vi) adsorption in simulated seawater environments.<sup>35,36</sup> The experimental results are shown in Fig. 8A. Specifically, in the experiment, 50 mg of aerogel beads were used to adsorb U(vi) from seawater samples of different volumes, each containing 3.3 μg L<sup>-1</sup> of U(vi). The experimental results indicated that the maximum adsorption capacity of this composite aerogel reached 3.96 mg g<sup>-1</sup>. Furthermore, as shown in Fig. 8B, the

Table 3 Comparison of adsorption properties between this study and previous reports on MXenes adsorption of U(vi)

Adsorbent	Initial pH	Equilibrium time (min)	Maximum adsorption capacity (mg g <sup>-1</sup> )	References
Ti <sub>3</sub> C <sub>2</sub> T <sub>x</sub>	5	150	174	10
Ti <sub>2</sub> CT <sub>x</sub>	3	2880	470	11
Ti <sub>3</sub> C <sub>2</sub> T <sub>x</sub> -TCCH	4	120	334	12
Ti <sub>3</sub> C <sub>2</sub> T <sub>x</sub> @biochar	7	180	239.7	30
LDHs-Ti <sub>3</sub> C <sub>2</sub> T <sub>x</sub>	5	180	241	31
Amino-Ti <sub>3</sub> C <sub>2</sub> T <sub>x</sub>	5	120	278	32
HPC/Ti <sub>3</sub> C <sub>2</sub> T <sub>x</sub> /POSS	5	120	307	33
Carboxyl-Ti <sub>3</sub> C <sub>2</sub> T <sub>x</sub>	5.3	120	345	34
TiVCT <sub>x</sub>	5.3	60	336	This work

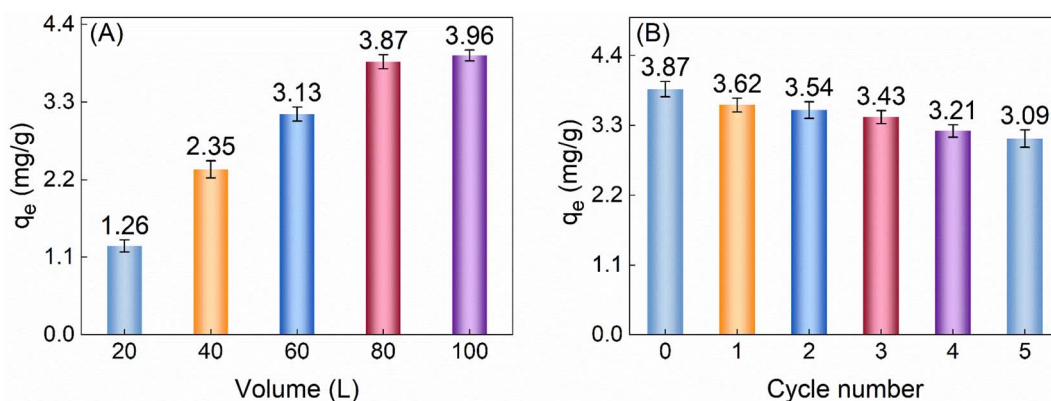


Fig. 8 (A)  $q_e$  of 50 mg aerogel for low concentration U(vi) in simulated seawater of different volumes; (B)  $q_e$  of 50 mg for 80 L seawater can be reused.



aerogel beads demonstrated good recyclability, with their adsorption capacity remaining above 80% of the initial value after five cycles of reuse.

## 4. Conclusion

In this study, an ultrathin nano-layered adsorbent, TiVCT<sub>x</sub>, was successfully synthesized, and a simple freeze-drying method was employed to combine it with sodium alginate, resulting in easily recoverable aerogel spheres. TiVCT<sub>x</sub> exhibited a high adsorption capacity for U(VI) in high-concentration wastewater, with a saturation adsorption capacity of 336 mg g<sup>-1</sup>. The adsorption mechanism was thoroughly analyzed, revealing electrostatic adsorption of U(VI) by TiVCT<sub>x</sub> based on zeta potential test results. Additionally, XPS analysis indicated a reduction adsorption mechanism involving the combined action of Ti and V on U(VI). The coexistence of electrostatic and reduction adsorption mechanisms contributed to TiVCT<sub>x</sub>'s leading adsorption capacity among MXene materials. Furthermore, in simulated seawater with a U(VI) concentration of only 3.3 μg L<sup>-1</sup>, the TiVCT<sub>x</sub> aerogel spheres demonstrated the ability to adsorb U(VI) from complex environments, achieving an adsorption capacity of 3.96 mg g<sup>-1</sup>. This research not only provides an efficient adsorbent material but also offers important practical insights into the application of MXene in U(VI) adsorption. TiVCT<sub>x</sub> has demonstrated superior adsorption performance and ion interference resistance in experimental settings, indicating its broad potential for the adsorption of U(VI) in seawater. There is significant room for improvement in the application exploration of U(VI) under simulated seawater conditions, and we will continue to delve deeper into this issue in subsequent research.

## Data availability

All data included in this study are available upon request by contact with the corresponding author.

## Conflicts of interest

There are no conflicts to declare.

## Acknowledgements

This study was funded by Fundamental Science on Nuclear Wastes and Environmental Safety Laboratory. We also thank the Shiyanjia Lab for conducting XRD, ICP, and SEM tests.

## References

- N. Mahmood, Danish, Z. Wang and B. Zhang, *Nucl. Eng. Technol.*, 2020, **52**, 1327–1333.
- L. Guo, L. Peng, J. Li, W. Zhang and B. Shi, *J. Cleaner Prod.*, 2023, **388**, 136006.
- X. Li, D. Zeng, Z. He, P. Ke, Y. Tian and G. Wang, *Carbohydr. Polym.*, 2022, **276**, 118729.
- J. Chen, L. Xia and Q. Cao, *J. Hazard. Mater.*, 2022, **434**, 128893.
- A. Bhandari, *J. Magn. Magn. Mater.*, 2022, **548**, 168975.
- H. Li, J. Song, C. Ma, C. Shen, M. Chen, D. Chen, H. Zhang and M. Su, *J. Environ. Manage.*, 2024, **349**, 119347.
- S. Shi, R. Wu, S. Meng, G. Xiao, C. Ma, G. Yang and N. Wang, *J. Hazard. Mater.*, 2022, **436**, 128983.
- N. M. Tran, Q. Hoai Ta, A. Sreedhar and J. S. Noh, *Appl. Surf. Sci.*, 2021, **537**, 148006.
- D. A. Giannakoudakis, I. Anastopoulos, M. Barczak, E. Antoniou, K. Terpiłowski, E. Mohammadi, M. Shams, E. Coy, A. Bakandritsos, I. A. Katsoyiannis, J. C. Colmenares and I. Pashalidis, *J. Hazard. Mater.*, 2021, **413**, 125279.
- L. Wang, W. Tao, L. Yuan, Z. Liu, Q. Huang, Z. Chai, J. K. Gibson and W. Shi, *Chem. Commun.*, 2017, **53**, 12084–12087.
- L. Wang, H. Song, L. Yuan, Z. Li, Y. Zhang, J. K. Gibson, L. Zheng, Z. Chai and W. Shi, *Environ. Sci. Technol.*, 2021, **52**, 10748–10756.
- P. Zhang, L. Wang, K. Du, S. Wang, Z. Huang, L. Yuan, Z. Li, H. Wang, L. Zheng, Z. Chai and W. Shi, *J. Hazard. Mater.*, 2020, **396**, 122731.
- Y. S. Zhao, C. X. Liu, M. Feng, Z. Chen, S. Q. Li, G. Tian, L. Wang, J. B. Huang and S. J. Li, *J. Hazard. Mater.*, 2010, **176**, 119–124.
- J. W. Bai, X. F. Ma, C. Gong, Y. M. Chen, H. J. Yan, K. W. Wang and J. Wang, *J. Mol. Liq.*, 2020, **320**, 114443.
- K. R. G. Lim, M. Shekhirev, B. C. Wyatt, B. Anasori and G. Yury, *Nat. Synth.*, 2022, **1**, 601–614.
- X. H. Li, S. S. Li, X. Cui, R. Zhang and H. Cui, *Appl. Surf. Sci.*, 2021, **563**, 150264.
- S. Kim, F. Gholamirad, M. Yu, C. Park, A. Jang, M. Jang, N. Taheri-Qazvini and Y. Yoon, *Chem. Eng. J.*, 2021, **406**, 126789.
- B. Jun, C. M. Park, J. Heo and Y. Yoon, *J. Environ. Manage.*, 2020, **256**, 109940.
- H. Wang, F. Wu, Z. Wang, Y. Wang, S. Zhang, H. Luo, Z. Zheng and L. Fang, *Chemosphere*, 2022, **308**, 136573.
- P. Karthikeyan, K. Ramkumar, K. Pandi, A. Fayyaz, S. Meenakshi and C. M. Park, *Ceram. Int.*, 2021, **47**, 3692–3698.
- Y. Feng, H. Wang, J. Xu, X. Du, X. Cheng, Z. Du and H. Wang, *J. Hazard. Mater.*, 2021, **416**, 125777.
- T. Habib, X. Zhao, S. A. Shah, Y. X. Chen, W. Sun, H. An, J. L. Lutkenhaus, M. Radovic and M. J. Green, *npj 2D Mater. Appl.*, 2019, **3**, 89.
- B. Jun, S. Kim, H. Rho, C. Park and Y. Yoon, *Chemosphere*, 2020, **254**, 126827.
- H. Xue, X. Gao, M. K. Seliem, M. Mobarak, R. Dong, X. Wang, K. Fu, Q. Li and Z. Li, *Chem. Eng. J.*, 2023, **451**, 138735.
- X. Wang, A. Zhang, M. Chen, M. K. Seliem, M. Mobarak, Z. Diao and Z. Li, *Chem. Eng. J.*, 2023, **473**, 145385.
- K. Li, T. Xiong, J. Liao, Y. Lei, Y. Zhang and W. Zhu, *Chem. Eng. J.*, 2022, **433**, 134449.
- D. Zhang, L. Liu, B. Zhao, X. Wang, H. Pang and S. Yu, *Environ. Pollut.*, 2023, **317**, 120826.



- 28 C. Zhang, Y. Wang, Y. Liu, Q. Zeng, Y. Wen, L. Guo, H. Chen, X. Xie and Q. Zeng, *Chem. Eng. J.*, 2024, **485**, 149856.
- 29 C. Peng, X. Li, P. Jiang, W. Peng, J. Tang, L. Li, L. Ye, S. Pan and S. Chen, *J. Hazard. Mater.*, 2022, **440**, 129740.
- 30 L. Chen, M. Wakeel, T. Haq, C. Chen and X. Ren, *J. Hazard. Mater.*, 2022, **430**, 128377.
- 31 S. Wang, L. Wang, Z. Li, P. Zhang, K. Du, L. Yuan, S. Ning, Y. Wei and W. Q. Shi, *J. Hazard. Mater.*, 2021, **408**, 124949.
- 32 F. Liu, S. Wang, C. Zhao and B. Hu, *Biochar*, 2023, **5**, 31.
- 33 P. Gu, S. Zhang, R. Ma, M. Sun, S. Wang, T. Wen and X. Wang, *Sep. Purif. Technol.*, 2022, **288**, 120641.
- 34 Y. Liu, X. Cheng, S. Liu, X. Dichen, Q. Chen, L. Wang and P. Gu, *Sep. Purif. Technol.*, 2022, **303**, 122216.
- 35 W. Zhao, H. Chi, X. Zhang, Y. Wang and T. Li, *Colloids Surf., A*, 2022, **650**, 129610.
- 36 P. Zhang, L. Wang, K. Du, S. Wang, Z. Huang, L. Yuan, Z. Li, H. Wang, L. Zheng, Z. Chai and W. Shi, *J. Hazard. Mater.*, 2020, **396**, 122731.

